

Title: Granular column collapse: Analysing the effects of gravity levels

Yucheng Li*	li@gut.rwth-aachen.de	Institute of Geotechnical and Underground Technology, RWTH Aachen University
Bowen Wang	B.Wang@gut.rwth-aachen.de	Institute of Geotechnical and Underground Technology, RWTH Aachen University
Raul Fuentes	raul.fuentes@gut.rwth-aachen.de	Institute of Geotechnical and Underground Technology, RWTH Aachen University

* Corresponding author

This manuscript is a non-peer reviewed preprint submitted to EarthArXiv.

Please note that it has been submitted to Computers and Geotechnics and is currently under review.

If you are interested in our findings or have questions, please feel free to contact any of the authors; we welcome feedback.

Computers and Geotechnics

Granular column collapse: Analysing the effects of gravity levels

--Manuscript Draft--

Manuscript Number:	COMGE-D-24-03411
Article Type:	Research Paper
Keywords:	Granular column collapse; Gravity level; Aspect ratio; Smoothed Particle Hydrodynamics
Corresponding Author:	Yucheng Li RWTH Aachen University Chair of Geotechnical Engineering and Institute of Geomechanics and Underground Technology Aachen, NonUS/Other GERMANY
First Author:	Yucheng Li
Order of Authors:	Yucheng Li Bowen Wang Raul Fuentes
Abstract:	<p>In this study, we investigated the effect of gravity level on the collapse of granular column using the Smoothed Particle Hydrodynamics (SPH) method based on the Mohr-Coulomb model. After validating the model with existing experimental studies, a dimensional analysis of the system's scaling factors was performed to evaluate the influence of varying gravity levels. The results show that gravity significantly influences collapse dynamics, particularly in shortening the collapse time. To predict collapse time, we propose two models that account for varying gravity acceleration (g), both of which scale positively with $N^{-1/2}$ ($g = NG$, where N is the gravity scaling factor, $G = 9.81\text{m/s}^2$). We find that the non-dimensional collapse time, $[[EQUATION]]$ (where $[[EQUATION]]$ is the collapse time, and $[[EQUATION]]$, with $[[EQUATION]]$ representing the initial height), is influenced by the initial aspect ratio, a (defined as $[[EQUATION]]$, where r_0 is initial radius of the column). While gravity does impact collapse dynamics, its effects on the deposit run-out distance and final height remain consistently scaled at 1.0 across varying gravity levels. Additionally, we propose a modified mobility angle, $[[EQUATION]]$, to investigate the effect of gravity on flow mobility, which aligns with expected gravity scaling. Furthermore, our findings are supported by observations of natural landslides in the Solar System. A multiscale analysis reveals that the spreading range of collapse is contingent on the sample volume and initial potential energy as opposed to gravity. This study provides insights for in-depth investigations into the collapse mechanism of granular materials in planetary exploration.</p>
Suggested Reviewers:	<p>Teng Man Zhejiang University of Technology manteng@westlake.edu.cn He has done a lot of work on granular materials, especially on granular material collapse.</p> <p>Jiayan Nie associate researcher, Wuhan University njiayan_@whu.edu.cn His research focuses on exploring the salient static, transient, and flow behaviors of granular materials by means of the theoretical model, physical test, discrete element method, and hierarchical multi-scale model.</p>
Opposed Reviewers:	

[Click here to view linked References](#)

Granular column collapse: Analysing the effects of gravity levels

Yucheng Li*; Bowen Wang; Raul Fuentes

Institute of Geomechanics and Underground Technology, RWTH Aachen University, 52074 Aachen, Germany

*Corresponding author at: Institute of Geotechnical and Underground Technology, RWTH Aachen University, 52074 Aachen, Germany. E-mail address: li@gut.rwth-aachen.de (Yucheng Li). ORCID: 0009-0001-7806-1415

ABSTRACT

In this study, we investigated the effect of gravity level on the collapse of granular column using the Smoothed Particle Hydrodynamics (SPH) method based on the Mohr-Coulomb model. After validating the model with existing experimental studies, a dimensional analysis of the system's scaling factors was performed to evaluate the influence of varying gravity levels. The results show that gravity significantly influences collapse dynamics, particularly in shortening the collapse time. To predict collapse time, we propose two models that account for varying gravity acceleration (g), both of which scale positively with $N^{-1/2}$ ($g = NG$, where N is the gravity scaling factor, $G = 9.81\text{m/s}^2$). We find that the non-dimensional collapse time, t_{∞}/τ_c (where t_{∞} is the collapse time, and $\tau_c = \sqrt{h_0/g}$, with h_0 representing the initial height), is influenced by the initial aspect ratio, a (defined as $a = h_0/r_0$, where r_0 is initial radius of the column). While gravity does impact collapse dynamics, its effects on the deposit run-out distance and final height remain consistently scaled at 1.0 across varying gravity levels. Additionally, we propose a modified mobility angle, θ' , to investigate the effect of gravity on flow mobility, which aligns with expected gravity scaling. Furthermore, our findings are supported by observations of natural landslides in the Solar System. A multiscale analysis reveals that the spreading range of collapse is contingent on the sample volume and initial potential energy as opposed to gravity. This study provides insights for in-depth investigations into the collapse mechanism of granular materials in planetary exploration.

Keywords: Granular column collapse, Gravity level, Aspect ratio, Smoothed Particle Hydrodynamics

MANUSCRIPT submitted to Computers and Geotechnics

Authors: Yucheng Li et al.

1 Introduction

The flow of granular materials is widely encountered in nature and industry, playing a crucial role in various scenarios, such as the design of slopes, snow and rock avalanche risk assessment, ore mining and transshipment, and the movement of grain in agriculture. In these applications, an in-depth understanding of the collapse mechanisms and characterisation of granular flows is essential for effective disaster prevention and risk management.

A traditional and simple test to understand the collapse behaviour of granular flow is the granular column collapse. Lube et al. (2004) and Lajeunesse et al. (2004) conducted seminal simple experiments. They filled a cylindrical column with granular materials and allowed them to spread over a horizontal surface under gravity. Their results revealed that the collapse characteristics (e.g., flow pattern, run-out distance, and final height) are mainly, although not uniquely, governed by initial aspect ratio, a . Depending on the value of initial aspect ratio, two distinct regimes can be distinguished in terms of the run-out distance. When a is low, the flow exhibits a regime dominated by friction. In this regime, the column's edges fall while leaving its inner part relatively undisturbed. Notably, during this stage, a simple linear relation between the deposit run-out distance and the initial aspect ratio is commonly reported (Lube et al., 2004, Lajeunesse et al., 2004, Szewc, 2017). However, as a increases, the governing mechanism of granular flow changes. The shear plane gradually shifts inwards until the entire free surface collapse. The spreading of granular flow is influenced by the pressure gradient. In this regime, the deposit run-out distance follows a different relationship with aspect ratio, specifically a power law relationship. The final deposit for samples with low a exhibit a truncated cone shape in three dimensions (3D) or a trapezoid shape in two dimensions (2D), whereas models with high a trend to result in conical or triangular-shaped deposits. The effect of many other parameters have been investigated like initial column porosity (Fern and Soga, 2016), particle shape (Tapia-McClung and Zenit, 2012, Wei et al., 2018, Hoang and Nguyen, 2023), inter-particle friction (Lai et al., 2023), particle size (Lai et al., 2017, Cabrera and Estrada, 2021, Su et al., 2022), grain size effects (Warnett et al., 2014, Cabrera and Estrada, 2019, Man et al., 2021b), cohesive materials collapse (Jing et al., 2018a, Zhu et al., 2022), collapse in water (Thompson and Huppert, 2007, Jing et al., 2018b, Polanía et al., 2022). Investigations have also been conducted to analysis the effect of boundary geometry parameters, such as an erodible surface (Crosta et al., 2009, Mangeney et al., 2010), air fluidization (Roche et al., 2011), lateral wall width (Zhang et al., 2021), cross-section shape (Teng Man, 2022) or basal friction (Li et al., 2024) of the granular column collapse. Although they have an influence on some of the characteristics and kinematics of granular collapse, the aspect ratio remains the dominating factor.

As space exploration advances, the prospect of utilizing resources from other planets and human colonisation is becoming increasingly viable. Humanity's understanding of outer planets is poised to expand significantly with ongoing national space programs, including National Aeronautics and Space

63 Administration (NASA) 's Artemis program, which aims to return to the moon and send astronauts to
64 Mars. On 15 May 2021, China's Zhu Rong rover successfully landed on Mars, making China as the
65 second country to operate a Mars rover. Through these endeavours, humanity has deepened its
66 understanding of space and the origins of planets. In terms of research, understanding the properties of
67 granular material (e.g., angle of repose, collapse behaviour) under varying gravity levels is crucial for
68 space exploration. Several studies have investigated the dependence of the dynamic angle of repose on
69 gravity; however, no broad consensus exists. While P. G. Hofmeister (2009) and Kleinhans et al. (2011)
70 demonstrated a dependence on gravity, Nakashima et al. (2011) and Atwood-Stone and McEwen (2013)
71 found no such relationship. The controversy was addressed by Marshall et al. (2018), whose classical
72 passive Earth pressure experiments conducted during reduced gravity flights showed that the angle of
73 repose is independence of gravity. Inspired by these previous studies on the angle of repose tests, we
74 focus on the collapse behaviour of granular materials. The first models for granular flows in centrifuge
75 systems were based on granular flow in a rotating drum (Arndt et al., 2006). Recent research has
76 expanded these flow configurations to include sliding down on curved channels (Bowman et al., 2010,
77 Gue. et al., 2010) and studying the flow rate during the discharge of a silo (Dorbolo et al., 2013). Cabrera
78 and Wu (2017) investigated the dynamic of granular flows under centrifugal acceleration, revealing that
79 as the slope angle and equivalent centrifuge acceleration increase, the flow velocity increase and flow
80 height decreases asymptotically until a constant height. Compared to experimental studies, numerical
81 simulations offer a more economical and accessible approach for investigating the effect of varying
82 gravity levels. Cabrera et al. (2020) investigated the scaling principles for granular flow in a centrifugal
83 acceleration field using discrete element method (DEM). Results show that granular flows scale
84 consistently only when the Coriolis acceleration is negligible, and are severely altered otherwise.

85 To our knowledge, there is no study that has systematically explored the effect of gravity levels on
86 granular column collapse. Consequently, the objective of the paper is to analyse the effects of varying
87 gravity levels on the collapse of gravity-driven particle column. After validating our model against
88 existing experimental studies, we conduct a comprehensive analysis of the scaling relationship between
89 gravity levels and collapse responses. By comparing our simulations results with natural landslides in
90 the Solar System, ranging from laboratory to large-scale scenarios, we establish a regression line that
91 supports our conclusions.

92 This work is structured as follows: Section 2 introduces the SPH theory and outlines the model set-up,
93 followed by the validation of the SPH model using experiments data from the literature. Section 3
94 presents the results regarding the influence of gravity levels on deposit profiles. This includes the flow
95 patterns, scaling laws for collapse time, deposit run-out distance & final height, and flow mobility.
96 Section 4 delves into the reasons of gravity effect on the collapse range. The final section comprises the
97 conclusions of this paper.

98 **1.1 SPH framework for the simulation of granular flow**

99 Due to the mesh-free nature of the method and the continuous media-based characteristics, the
 100 Smoothed Particle Hydrodynamics (SPH) method has been broadly demonstrated for the modelling of
 101 large deformation problems including granular column collapse (Chen and Qiu, 2012, Szewc, 2017,
 102 Fávvero and Borja, 2018, Kermani and Qiu, 2018, Yang et al., 2020, Bui and Nguyen, 2021). In SPH, a
 103 continuum domain is discretised into an assembly of particles, each of which possesses field variables
 104 (such as velocity and stress) and moves with its own velocity. The field variables are then calculated
 105 through a kernel approximation, as shown in Fig. 1. The equations are presented using the Einstein
 106 convention, where $\alpha, \beta,$ and γ denote the Cartesian coordinates.

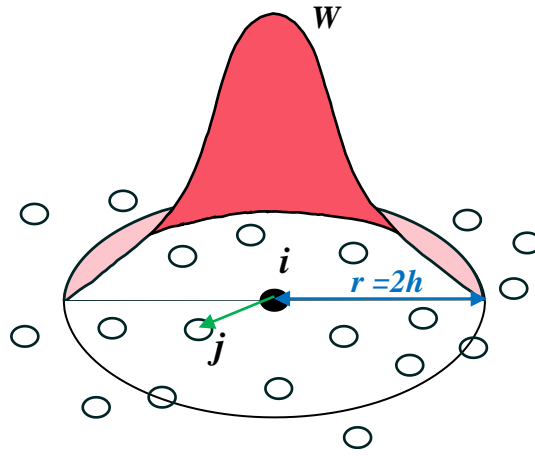


Fig. 1. Smoothing kernel function $W(\mathbf{x}, h)$ for particle i

109 The integral approximation of spatial function $f(\mathbf{x})$ at the point \mathbf{x} is defined as,

$$\langle f(\mathbf{x}) \rangle = \int_{\Omega} f(\mathbf{x}') W(\mathbf{x} - \mathbf{x}', h) d\mathbf{x}', \quad (1)$$

110 where Ω is the interpolation region, f is a function of the location vector \mathbf{x} of the particle, and $d\mathbf{x}$ is a
 111 volume. $W(\mathbf{x}, h)$ is kernel function, where h is the smoothing length.

112 The discrete form of Eq. (1) can be written as,

$$\langle \nabla \cdot f(\mathbf{x}) \rangle = \int_{\Omega} [\nabla \cdot f(\mathbf{x}')] W(\mathbf{x} - \mathbf{x}', h) d\mathbf{x}', \quad (2)$$

113 $W(\mathbf{x}, h)$ is defined using the function θ though the relation,

$$W(\mathbf{x}, h) = \frac{1}{h(x)^d} \theta(q), \quad (3)$$

114 where d is the number of space dimensions, and q is the relative distance, $q = |\mathbf{x} - \mathbf{x}'|/h$. $\theta(q)$ is the
 115 most commonly function cubic B-spline function and defined as,

$$\theta(q) = C \begin{cases} 1 - \frac{3}{2}q^2 + \frac{3}{4}q^3, & 0 \leq q \leq 1 \\ \frac{1}{4}(2 - q)^3, & 1 \leq q \leq 2, \\ 0, & \text{otherwise} \end{cases} \quad (4)$$

where C is a constant of normalization that depends on the number of the space dimensions.

Converting integral representations (as given in Eqs. (1) and (2)) into a particle approximation form:

$$\langle f(\mathbf{x}_i) \rangle = \sum_{j=1}^N \frac{m_j}{\rho_j} f(\mathbf{x}_j) W(\mathbf{x}_i - \mathbf{x}_j, h), \quad (5)$$

$$\langle \nabla \cdot f(\mathbf{x}_i) \rangle = \sum_{j=1}^N \frac{m_j}{\rho_j} f(\mathbf{x}_j) \nabla \cdot W(\mathbf{x}_i - \mathbf{x}_j, h), \quad (6)$$

where m_j is the mass of particle j , ρ_j is the density of particle j .

The general governing equations of mass and momentum conservation can be applied to granular material collapse as follows:

$$\frac{D\rho}{Dt} = -\rho \frac{\partial v^\alpha}{\partial x^\alpha}, \quad (7)$$

$$\frac{Dv^\alpha}{Dt} = \frac{1}{\rho} \frac{\partial \sigma^{\alpha\beta}}{\partial x^\beta} + b^\alpha, \quad (8)$$

where ρ is the material density; v^α is the velocity component; $\sigma^{\alpha\beta}$ is the stress tensor component; b^α is the acceleration due to the external forces.

The SPH approximation of governing equations can be derived using Eqs. (7) and (8). Writing partial differential governing equations in a discrete form. The mass conservation and momentum conservation in the framework of standard SPH becomes,

$$\frac{D\rho_i}{Dt} = \sum_{j=1}^N m_j (v_i^\alpha - v_j^\alpha) \frac{\partial W_{ij}}{\partial x_i^\alpha}, \quad (9)$$

$$\frac{Dv_i^\alpha}{Dt} = \frac{1}{\rho_i} \sum_{j=1}^N \frac{m_j}{\rho_j} (\sigma_i^{\alpha\beta} + \sigma_j^{\alpha\beta}) \frac{\partial W_{ij}}{\partial x_i^\beta} + b_i^\alpha, \quad (10)$$

where b_i^α is the force per unit mass due to gravitation. The Monaghan's type artificial viscosity is also implemented and shown in Appendix I.

To simulate the behaviour of the granular media we use a simple Mohr-Coulomb constitutive model where the yield surface and its plastic potential function are expressed as follows, respectively:

$$f = \sin \varphi I_1 + \frac{1}{2} [3(1 - \sin \varphi) \sin \theta + \sqrt{3}(3 + \sin \varphi) \cos \theta] \sqrt{J_2} - 3c \cos \varphi = 0, \quad (11)$$

$$g = \sin \psi I_1 + \frac{1}{2} [3(1 - \sin \psi) \sin \theta + \sqrt{3}(3 + \sin \psi) \cos \theta] \sqrt{J_2} - 3c \cos \psi, \quad (12)$$

130 where φ and ψ are the soil internal friction and dilatant angles, respectively; I_1 , J_2 , and J_3 are the first
 131 principal, second, and third deviatoric stress invariants, respectively; c is cohesion; and θ is the Lode
 132 angle, $\theta = \frac{1}{3} \cos^{-1}(1.5\sqrt{3} \frac{J_3}{J_2^{1.5}})$.

133 The general form of the elastic-perfectly plastic model is shown in Appendix. II.

134 To maintain the objectivity constitutive model under large deformation, the Jaumann stress tensor is
 135 adopted. The final form of the stress-strain relation for Mohr-Coulomb elastic-perfectly plastic
 136 constitutive model can be expressed by:

$$\dot{\sigma}^{\alpha\beta} = \sigma^{\alpha\gamma} \dot{\omega}^{\beta\gamma} + \sigma^{\gamma\beta} \dot{\omega}^{\alpha\gamma} + 2G \dot{e}^{\alpha\beta} + K \dot{\varepsilon}^{\gamma\gamma} \delta^{\alpha\beta} - \dot{\lambda} \left[3K \sin \varphi \delta^{\alpha\beta} + 2G \left(\frac{\partial g}{\partial J_2} s^{\alpha\beta} + \frac{\partial g}{\partial J_3} t^{\alpha\beta} \right) \right], \quad (13)$$

137 where $\dot{\varepsilon}^{\alpha\beta}$ and $\dot{\omega}^{\alpha\beta}$ are the strain and spin rate tensors, which can be related to the gradient of the
 138 velocity as follows:

$$\dot{\varepsilon}^{\alpha\beta} = \frac{1}{2} \left(\frac{\partial v^\alpha}{\partial x^\beta} + \frac{\partial v^\beta}{\partial x^\alpha} \right), \quad (14)$$

$$\dot{\omega}^{\alpha\beta} = \frac{1}{2} \left(\frac{\partial v^\alpha}{\partial x^\beta} - \frac{\partial v^\beta}{\partial x^\alpha} \right). \quad (15)$$

139 1.2 Model set-up

140 The dimensions of the granular column collapse model are shown in Fig. 2(a). It consists of a cylindrical
 141 domain placed over a rigid horizontal surface. The friction coefficient, μ , between the rigid plane and
 142 SPH particle was set to 0.4 in accordance with the validation experiments of Lube et al. (2004). Fig. 2
 143 (b), (c), and (d) illustrate a sensitivity analysis of different particle spacings ($\Delta p = 2.0, 3.0$ or 5.0 mm
 144 that represents the initial distance between adjacent particles) for an aspect ratio of 0.55. A red circle
 145 with a radius of 0.176 m was used as a standard reference size for better comparisons. Balancing
 146 computational cost and accuracy, the particle spacing, $\Delta p = 3.0$ mm was chosen for all simulations in
 147 this study.

148 The gravitational acceleration scaling factor, denoted as N (where $g = NG$, $N=1/6, 1/3, 1, 2$, and 10 , G
 149 $= 9.81\text{m/s}^2$), is a crucial parameter in the simulation. Only the column height and gravitational
 150 acceleration were changed, while the column radius ($r_0=0.1\text{m}$) remained constant. The material density,
 151 angle of friction, Poisson's ratio and Young's modulus were 2600 kg.m^{-3} , 37° , 0.3, and 6.0 MPa
 152 respectively. A wide range of granular column aspect ratios are presented in Table 1.

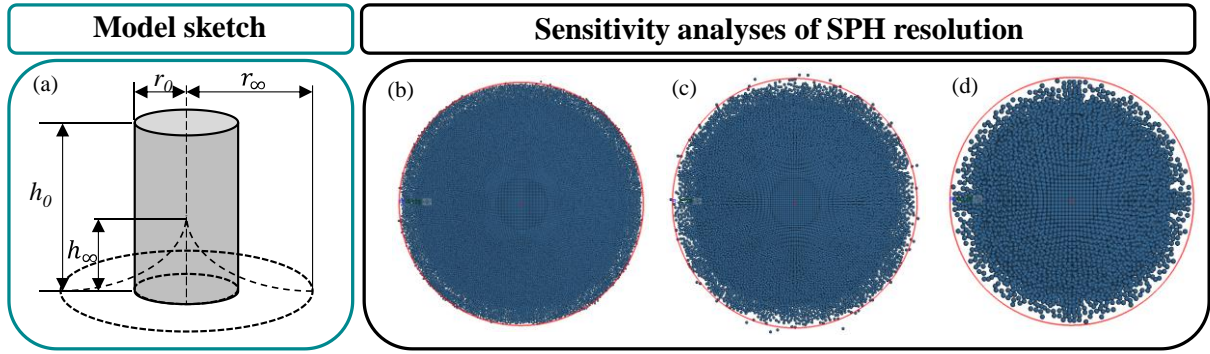


Fig. 2. (a) A sketch of the axisymmetric granular collapse: shaded region denotes the initial column (r_0 : initial radius, h_0 : initial height), dashed curve denotes deposit geometry (r_∞ : final run-out distance, h_∞ : final height). (b) Particle spacing ($a = 0.55$): $\Delta p = 2.0\text{mm}$ & 220,080 SPH particles. (c) $\Delta p = 3.0\text{mm}$ & 63,378 SPH particles. (d) $\Delta p = 5.0\text{mm}$ & 13,904 SPH particles.

Table 1. Series of example granular column collapse.

Case ID	$a = h_0/r_0$	h_0/m	No. of particles
1	0.55	0.055	63,378
2	1.0	0.10	119,714
3	1.5	0.15	176,050
4	2.75	0.275	323,932
5	4	0.4	471,814
6	6	0.6	704,200
7	10	1.0	1,176,014
8	13.8	1.38	1,619,660
9	18	1.8	2,112,600
10	25	2.5	2,932,993

1.3 Model validation

The numerical model was validated against the experiments of Lube et al. (2004) under the Earth's gravitation acceleration ($G = 9.81\text{m/s}^2$), focusing on three key aspects: deposit pattern, run-out distance, and final height. Figure. 3 presents deposit patterns of numerical simulations and experimental results. Depending on the aspect ratio values results, three distinctly different deposit patterns are shown. For small aspect ratios (e.g., $a = 0.55$), a flat surface remains at the top of the model; for intermediate aspect ratios (e.g., $a = 2.75$), the top surface changes from a flat plate to a conical tip; for large aspect ratios (e.g., $a = 13.8$), the sand forms an outward propagating wave during the process, transferring mass from the centre to the edge of the diffusion. Our numerical flow patterns agree well with the experimental results (Lube et al., 2004, Lajeunesse et al., 2004) and numerical results (Man et al., 2021a, Sheikh et al., 2021).

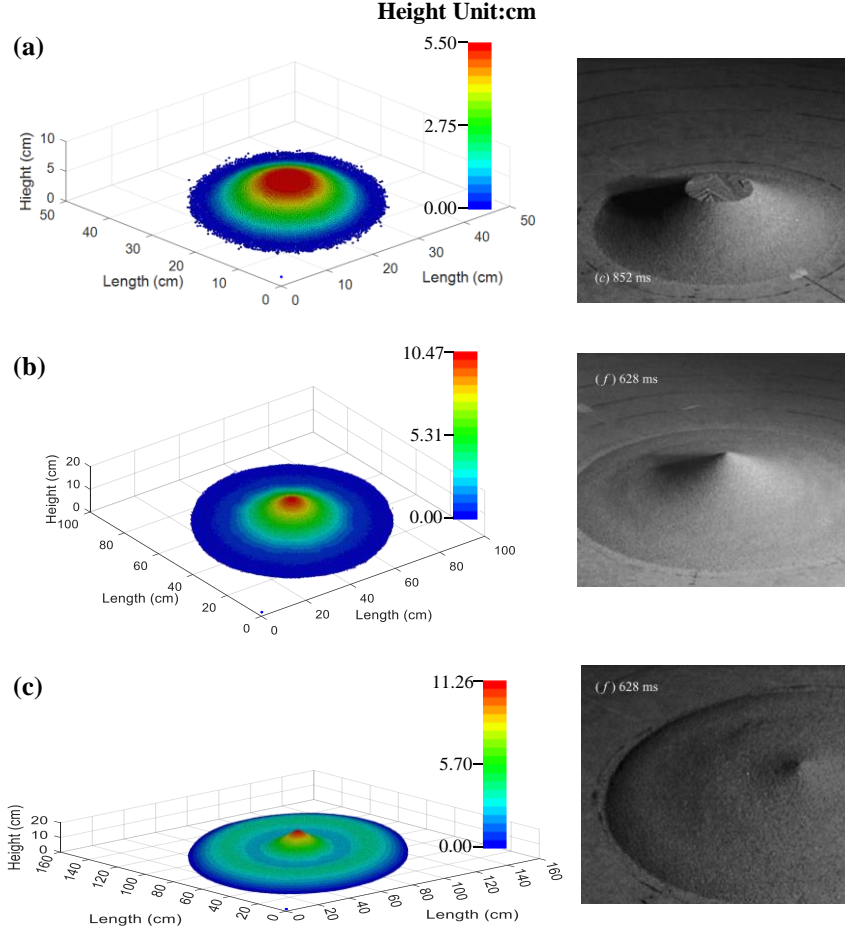


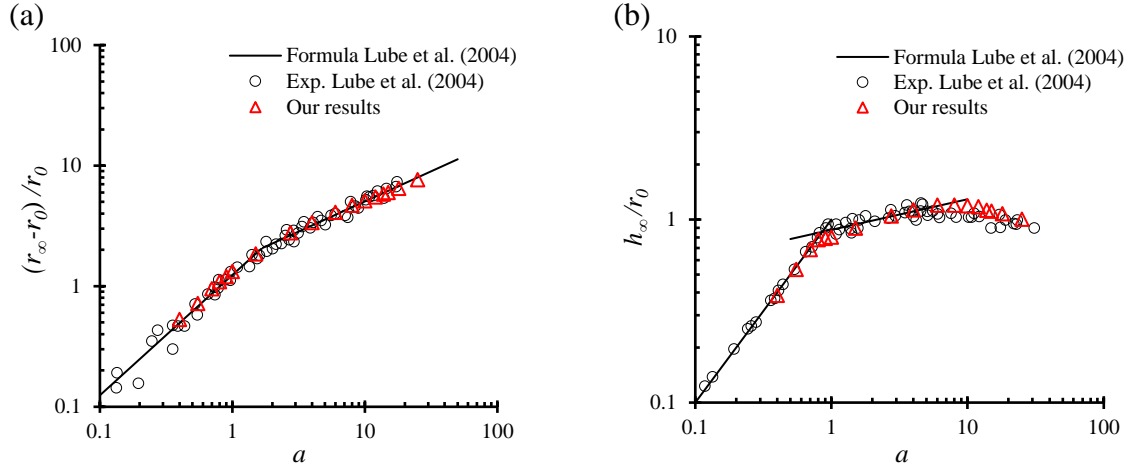
Fig. 3. Qualitative comparison of numerical (left images) and experimental results (right grey images) reported by Lube et al. 2004 of deposit profiles at three typically aspect ratios. (a) $a = 0.55$. (b) $a = 2.75$. (c) $a = 13.8$.

Figure. 4(a) shows the validation of the run-out distance. Our simulation results against well the experimental points and formula form (see Eq. (16)) of Lube et al. (2004).

Our results of final height, h_{∞} , are plotted in Fig. 4(b) and are in good agreement with the experimental and formula (Eq. (17)) results. The critical aspect ratio also fits also well with the 1.0 proposed by Lube et al. (2004). When the aspect ratio is less than 1.0, the model shows circular truncated cones pattern. The model maintains the initial height (e.g., $a = 0.55$, Fig. 3). The morphology becomes more complex when the aspect ratio exceeds 1.0 (e.g., $a = 2.75$ or $a = 13.8$, Fig. 3).

$$\frac{r_{\infty} - r_0}{r_0} = r^* \approx \begin{cases} 1.24a, & a < 1.7 \\ 1.6a^{1/2}, & a \geq 1.7 \end{cases} \quad (16)$$

$$\frac{h_{\infty}}{r_0} = h^* = \begin{cases} a, & 0 \leq a < 1.0 \\ 0.88a^{1/6}, & 1.0 \leq a < 10 \end{cases} \quad (17)$$



181 Fig. 4. The relationship between rescaled final height and initial aspect ratio. (a) run-out distance; (b) final height.

182 1.4 Assumption of scaling factors

183 Before analysing the results, we assume that the gravity level should obey certain scaling laws. To
 184 validate this assumption and extend it to other aspect ratios, and regimes, we conduct a scaling analysis
 185 of the problem, starting from a hypothesis that scaling derived from simple dimensional analysis is
 186 sufficient. The actual scaling factors of this hypothesis assume a scaling N of gravity and a scaling of
 187 1.0 for density and length. This leads to the overall scaling factors shown in Table 2. In the following
 188 sections, we will compare these values with those in the literature and our obtained results.

189 Table 2. Scaling factors assuming a simple dimensional analysis. *Indicates enforced scaling parameters in the
 190 system.

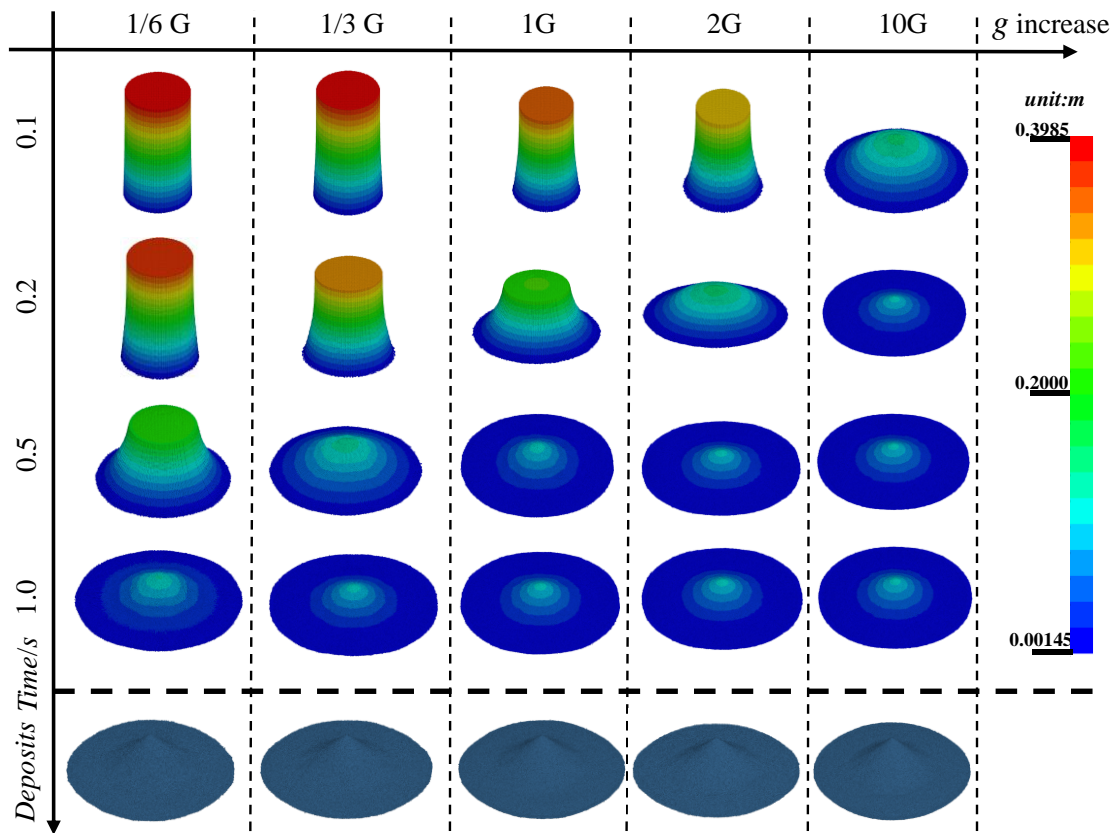
<i>Variable</i>	<i>Units</i>	<i>Scaling values</i>
L^*	m	1
ρ^*	kg/m^3	1
g^*	m/s^2	N
F	N	N
<i>Stress</i>	N/m^2	N
v	m/s	$N^{1/2}$
t	s	$N^{-1/2}$
<i>Energy</i>	J	N

191

192 **2 Results**

193 **2.1 Typical evolution of avalanche flow patterns**

194 In Fig. 5, a typical aspect ratio (e.g., $a = 4$) was used to demonstrate the effect of gravity levels on the
 195 evolution of flow patterns. As expected, higher gravity levels accelerate the collapse process. This is
 196 consistent with the conclusion of Meruane et al. (2010), who claimed that the flow velocity and duration
 197 of emplacement are gravity dependent. Additionally, we initially find that the varying gravity levels
 198 produce same deposit morphologies (bottom row of Fig. 5). This indicates that the gravity has a
 199 significant influence on the dynamics of the collapse of granular column but no impact on the deposit
 200 morphology.



201
 202 Fig. 5. Snapshots of granular column collapse at different gravity levels. The bottom blue pictures are final deposit
 203 morphologies.

204 **2.2 Collapse time prediction models**

205 **2.2.1 Scaling by the initial geometry**

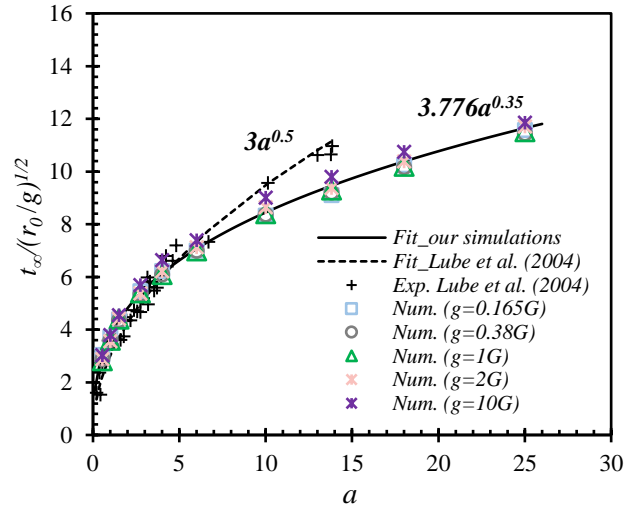
206 The relationship between scaling factor (N) of varying gravity and the collapse time of granular column
 207 was investigated. Lube et al. (2004) investigated scenarios with the same gravitational acceleration (g)

208 but different initial radius ($r_0 = 2.9, 7.5,$ and 9.7cm). Their findings indicated that different r_0 has no
 209 effect on the non-dimensional collapse time.

$$\frac{t_\infty}{\sqrt{r_0/g}} = f(a) \quad (18)$$

210 In this work, we keep r_0 constant while varying gravity levels to examine the effect of gravity on the
 211 collapse dynamics. Fig. 6 shows the non-dimensional collapse time and the scaling laws derived from
 212 our results. Our new correlation is shown in Eq. (19) with a value of $R^2 = 0.995$. This scaling by $1/\sqrt{g}$
 213 aligns with the observations of Lube et al. (2004) and their developed Eq. (18). Both our results and
 214 experimental of Lube et al. (2004) show an increasing trend in non-dimensional time as the aspect ratio
 215 increases. We observe a deviation for values of a larger than 5.0. The fit is satisfactory for $a < 5.0$, with
 216 discrepancies only present in scenarios with larger aspect ratios. This reason for this bias may be that
 217 they had insufficient data with larger aspect ratios in their experiments (their fitting form was mainly
 218 based on $a < 5.0$, with only 5 tests between $5.0 < a < 15.0$, and no cases with $a > 15.0$).

$$\frac{t_\infty}{\sqrt{r_0/g}} = 3.776 * a^{0.35} \quad (19)$$



219
 220 Fig. 6. The scaling laws of collapse time and the scaling laws obtained from regression analysis for different
 221 gravity levels.

222 2.2.2 Scaling by the characteristic time

223 Another approach for predicting collapse time was used based on the analysis of single-particle free fall,
 224 where $h = \frac{1}{2}gt^2$, then $t = \sqrt{2h/g}$. Here, by introducing the characteristic time scale τ_c ($\tau_c = \sqrt{h_0/g}$)
 225 to evaluate the collapse time, we derive Eq. (20) with $R^2=0.97$, and illustrate the fitted results in Fig. 7.

$$\frac{t_\infty}{\tau_c} = \frac{3.712}{a^{0.14}} \quad (20)$$

Lajeunesse et al. (2005) claimed that the propagation evolution can be differentiated into three sections. In the first section ($t < 0.8\tau_c$) the collapse process accelerates, resulting in the spreading of the deposit tip in a positive horizontal direction. Subsequently, the foot of the material propagates at nearly constant velocity for about $2\tau_c$. In the final section, the material propagation decreases until it reaches the final deposit position after approximately $0.6\tau_c$. They define approximately $3\tau_c$ as a guide value for the total duration of the collapse. However, our results show that the non-dimensional collapse time (t_∞/τ_c) is not a constant value, but it is also affected by the initial aspect ratio. Specifically, at lower aspect ratios ($a < 5.0$), the non-dimensional collapse time tends to decrease rapidly, and this trend diminishes as the aspect ratio increases. Based on Eq. (20), we calculated that the ratio of the collapse time to the free-fall time ($t_\infty/\sqrt{2h_0/g}$) of a single particle decreases as the aspect ratio increases (see the black dashed line in Fig. 7). This finding differs from that of Lube et al. (2004), who reported that the collapse time of granular materials in columns is approximately twice the free fall time (see the red dashed line in Fig. 7). The discrepancy may lie in the higher columns, whose collapse mechanism is predominantly influenced by pressure gradients, resulting in a short collapse time that tends to a free-fall state.

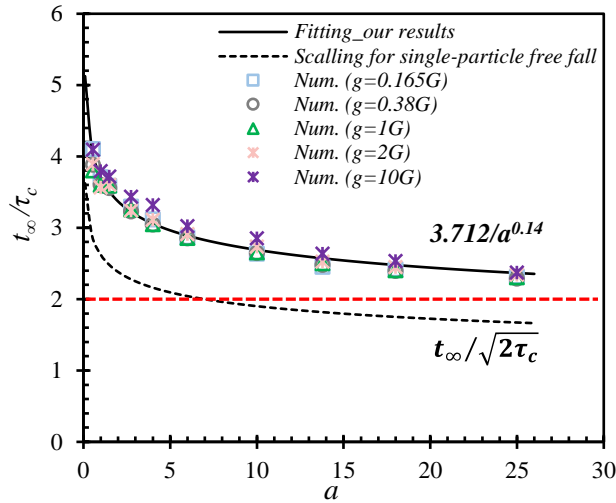


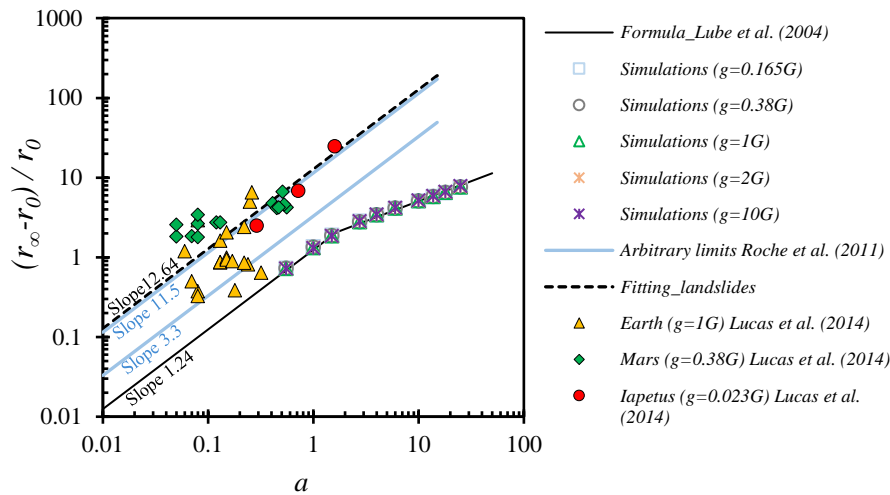
Fig. 7. Influence of gravity level on the collapse time normalized by the characteristic time. The black dashed line is the scaling line for single-particle free fall condition ($t_\infty/\sqrt{2\tau_c}$) derived from the regression analysis of simulation results (black line).

Eq. (19) or Eq. (20) can be easily compared. In both equations, the collapse time is positively correlated with $1/\sqrt{g}$, represented as $N^{-1/2}$, agreeing with previous studies that assumed scaling factors in Table 2. This suggests that we can use Eq. (19) or Eq. (20) to estimate the collapse time at different gravity levels, once knowing the necessary parameters.

248 2.3 Deposit run-out distance

249 Fig. 8 presents the correlation between run-out distance and aspect ratio at different gravity levels. The
 250 expected scaling of 1.0 (see Table 2) is clearly confirmed for the numerical results, indicating that the
 251 gravity level does not impact the normalized run-out distance. Moreover, the gravity level does not alter
 252 the critical aspect ratio at which the shift occurs in the bilinear relationship shown in Fig. 8. It remains
 253 a constant value at 1.7, as noted in Eq. (16).

254 Additionally, large-scale results, such as the natural landslides in Solar System (Lucas et al., 2014),
 255 present a regression line with a slope of 12.64 and $R^2=0.88$. Notably, the landslides on Mars and Iapetus
 256 also align well with this regression line, supporting our conclusion about the consistent effect of gravity
 257 on run-out distance across different celestial bodies. This finding is also consistent with the work of
 258 Roche et al. (2011), who normalized the run-out distance of the Valles Marineras (Lajeunesse et al.,
 259 2006, Lucas et al., 2011), delimited by blue dashed lines with slopes of 3.3 and 11.5 (see blue arbitrary
 260 lines in Fig. 8). While their results indicate a larger value compared to both our simulations and granular
 261 column experimental findings, it confirms the scaling. The differences in magnitude can be explained
 262 by the fact that natural landslides travel unexpectedly long distances, indicating lower dissipation during
 263 collapse, potentially induced by other mechanisms such as material entrainment or water lubrication.
 264 However, the precise physical processes underlying energy dissipation during natural granular flows
 265 remain uncertain (Lucas et al., 2014).

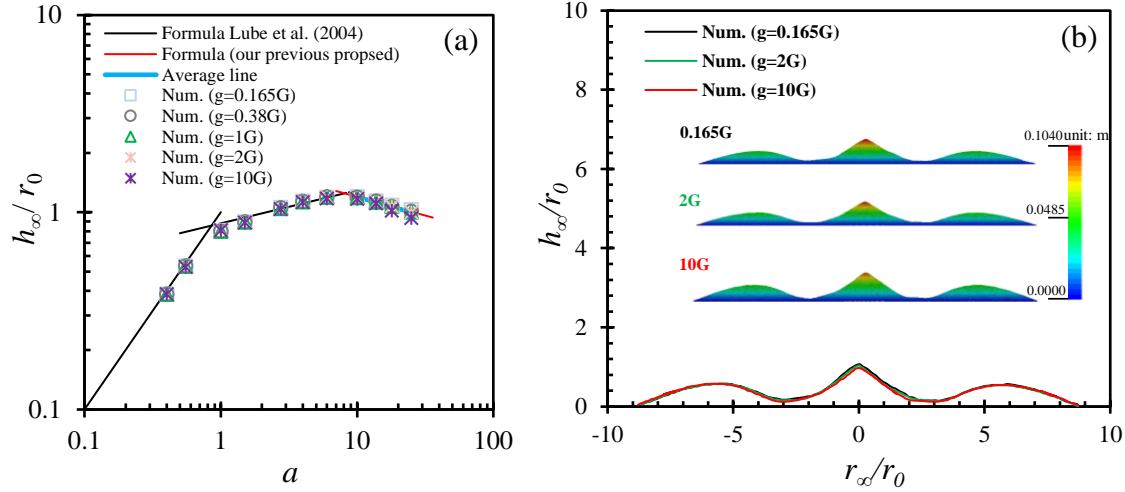


266
 267 Fig. 8. Influence of gravity level on the normalized run-out distance. The natural data of landslides in Earth, Mars,
 268 and Iapetus are referenced from Lucas et al. (2014).

269 2.4 Final height

270 Fig. 9(a) presents the rescaled final height at various aspect ratios. Again, the expected scaling of 1.0 is
 271 consistently observed across different aspect ratio ranges. The results also align well with our proposed

272 formula for final height when $a > 10$ (as indicated by the blue and red lines in the inset of Fig. 9(a)),
 273 with some nuances at high aspect ratios. To further analysis these differences in detail, we conducted a
 274 cross-sectional of deposit profiles for $a = 25$ (see Fig. 9(b)). The deposit morphology appears very
 275 similar, as depicted in the inset of Fig. 9(b). Notably, we observed a slightly lower final height under
 276 high gravity conditions (e.g., $g = 10G$), although the effect was negligible.



277
 278 Fig. 9. (a) The rescaled final height versus aspect ratio at different gravity conditions. (b) Deposit profiles $f(r, h)$
 279 normalized to the column radius. The deposit cross-section profiles of $a=25$ (height coordinates) at different
 280 gravity levels (0.165G, 2G, and 10G) are presented in the inset.

281 2.5 Flow mobility

282 The particles in dry granular flow under the driving force of gravity. It is very important to quantitatively
 283 analysis the effect of gravity levels on the flow mobility. The reciprocal of the granular flow mobility
 284 can be measured by the ratio of h_∞ and r_∞ (Cagnoli and Piersanti, 2015, Lai et al., 2017) in Eq. (21).
 285 The angle θ is referred to as the flow mobility angle (see the inset of Fig. 10). The higher the flow
 286 mobility of the flow, the smaller the angle. We introduced another mobility angle, θ' , in Eq. (22) where
 287 we normalise by the initial column radius. The angle is referred to as the modified flow mobility angle
 288 (see the inset of Fig. 10).

$$289 \tan\theta = h_\infty/r_\infty \quad (21)$$

$$290 \tan\theta' = h_\infty/(r_\infty - r_0) = h^*/r^* \quad (22)$$

291 It was observed that both θ and θ' decreases as the aspect ratio increases, following the expected scaling
 292 with the gravity level. However, θ exhibits a small peak point at $a \approx 1$, which is attributed to the effect
 293 of initial geometry. A straightforward validation, as depicted in the inset of Fig. 10(b), illustrates that
 when $a < 0.8$, the model, dominated by friction, maintains the initial height h_0 . As a increases, h_0
 increases more rapidly than r_∞ , leading to an increasing trend for θ . Only when $a \geq 0.8$, h_∞ decreases

with r_∞ , resulting in a lower θ . Conversely, θ' eliminates the effect of the initial geometry (r_0), and the curve undergoes continuous variation. As the aspect ratio increases, the initial geometry effect diminishes, eventually causing θ' to approach θ .

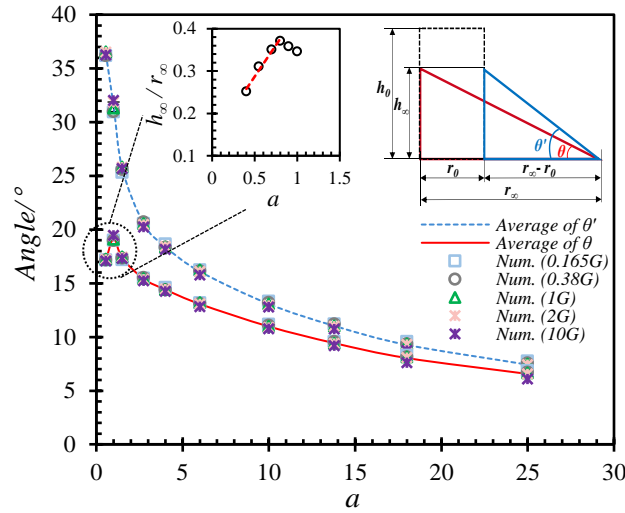
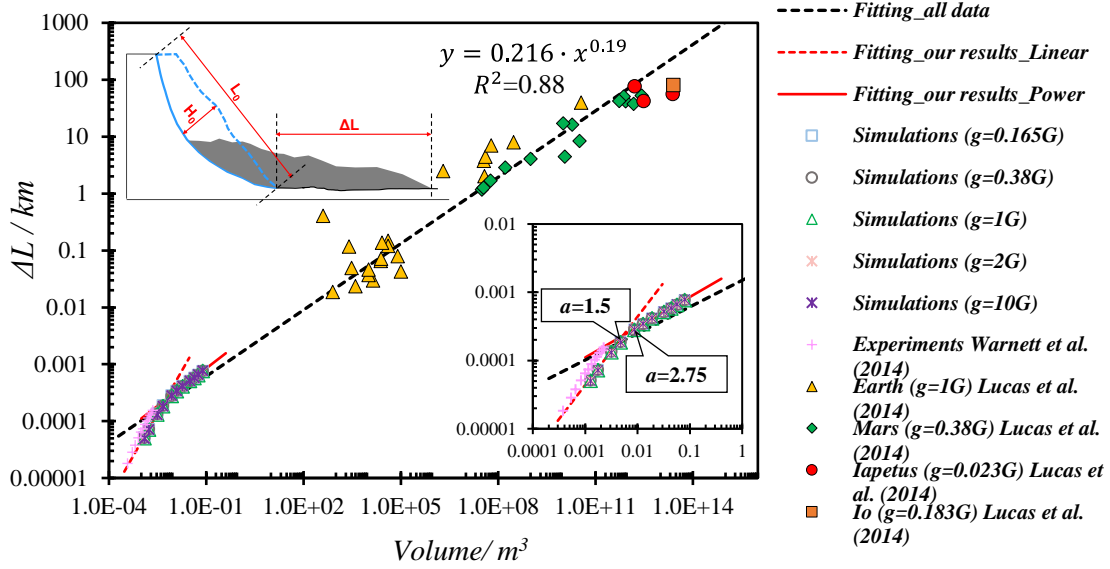


Fig. 10. The effect of gravity levels on the flow mobility. The sketch of mobility angle θ and θ' are shown in the inset. The inset also shows the validation results for model at $\mu = 0.4$ and $g = 1G$.

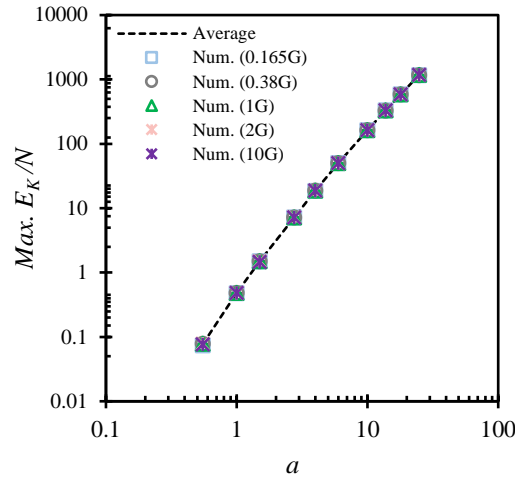
3 Discussion

Comparing experimental or simulation results with actual engineering data is essential for validating and refining the model, as well as for understanding its applicability in real-world scenarios. As depicted in Fig. 8, the aspect ratio of natural landslides typically falls well below 1.0 and in a much narrower range compared to experiments. Consequently, using aspect ratio as a criterion for analysing the large-scale landslides may not be suitable. Motivated by this, we investigated the effect of gravity level on the relationship between the length travelled (ΔL) and landslide initial volume, as shown in Fig. 11. The results suggest that the run-out distance is independent of gravity level, which is consistent for small-scale and large-scale slides. Through regression analysis, a critical point in volume was identified, corresponding to $1.5 \leq a \leq 2.75$. This critical point closely corresponding to the transition point of 1.7 identified by Lube et al. (2004). For volumes less than this critical point, our simulation results, along with experimental findings (Warnett et al., 2014), exhibit a linear increasing trend as volume increases. Conversely, for volumes greater than this critical point, our small-scale results fit well with large-scale landslide data, showing a power increase trend. This finding is consistent with previous research by Lajeunesse et al. (2005), who suggested that in lower columns, collapse is primarily influenced by friction, while in higher columns, it is governed by pressure gradients. The existence of this critical point also reflects the transition phase between the influence of slide volume effects on the spreading distance at small and large scales.

318 The maximum kinetic energy (E_K) under different gravity level also scales well with a scaling factor of
 319 N , as shown in Fig. 12. That further supports that the gravity level does not influence the deposit run-
 320 out distance.



321
 322 Fig. 11. The travel length (ΔL) as a function of initial volume. H_0 is the maximum initial thickness, L_0 the initial
 323 length and ΔL is the travel length by the front landslide. The inset figure illustrates the most frequent geometry
 324 for natural landslides, where the dashed blue region represents the initial geometry, and the grey region represents
 325 the deposit geometry. The volume corresponds to the aspect ratio point is depicted in the inset figure. The fitting
 326 formula for landslide data (Lucas et al., 2014) is also shown in the inset.



327
 328 Fig. 12. The maximum of kinetic energy E_K scaled by a factor of N at different aspect ratios.

329 Strom et al. (2019) also analysed the dependency of run-out distance or affected area on the product of
 330 $V \times H_{max}$, which is a proxy to initial potential energy. We compared our small-scale simulation results
 331 and the experimental findings of Warnett et al. (2014) with large-scale landslide data from the Solar

System (Lucas et al., 2014), as shown in Fig. 13. We constructed a best-fit regression line (depicted as a black dashed line), achieving an R^2 value of 0.87. This highlights the consistency of small-scale results with large-scale landslide data, emphasizing the significance of potential energy as a crucial factor influencing deposit run-out distance.

Moreover, the obtained regression line validates that the gravity level scales according to our proposed model scaling. Additionally, the total potential energy of our simulations aligns well with a scaling factor N across different aspect ratios, as illustrated in the inset of Fig. 13.

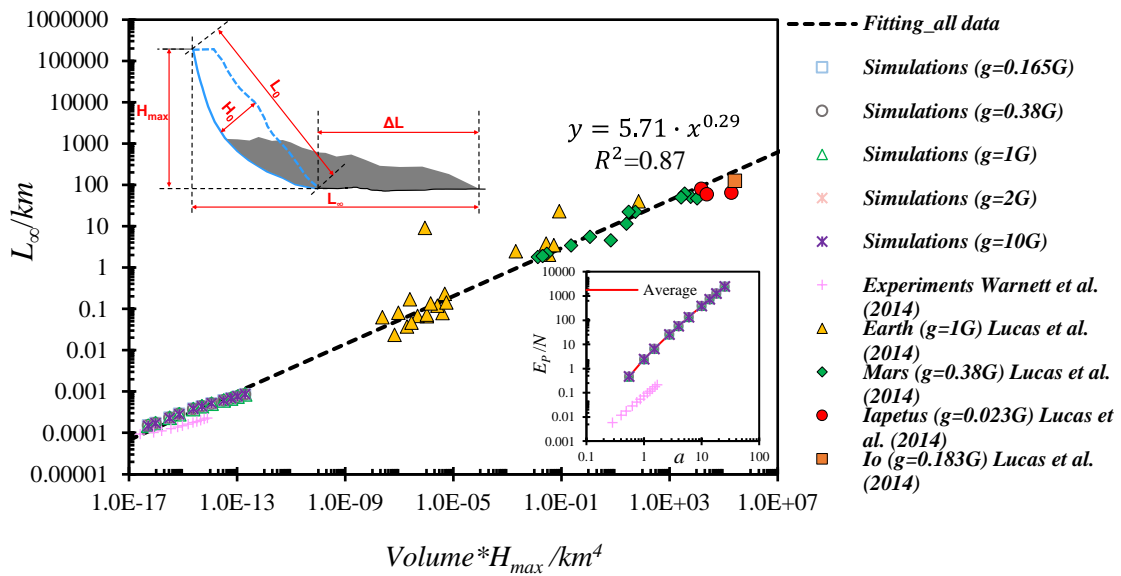


Fig. 13. Relationships between run-out distance and product of landslide volume and maximal height at different gravity conditions. H_{max} is the maximum elevation of the initial mass, H_0 is the maximum initial thickness and L_{∞} is the total travel length of the landslide.

4 Conclusions

In this study, we use the Smoothed Particle Hydrodynamics (SPH) model and literature results to investigate the effects of gravity conditions on gravity-driven particle column collapse. This research explores how varying gravity levels influence collapse behaviours through a scaling analysis of non-dimensional collapse time, deposit geometry, and energy analysis. The results are summarized as follows:

(1) Higher gravity levels significantly shorten the collapse time of granular column while maintaining similar deposit morphologies. This suggests that gravity levels play a significant role in the dynamics of collapse but have no impact on the deposit morphology.

(2) To accurately predict the collapse time of granular column, two models were proposed, each accounting for different gravity levels. Both models demonstrate a positive correlation with $1/\sqrt{g}$,

354 represented as $N^{1/2}$. We found that the non-dimensional collapse time (t_{∞}/τ_c) is not a constant but
1 355 influenced by the initial aspect ratio. We also found that the ratio of the collapse time to the free-fall
2
3 356 time ($t_{\infty}/\sqrt{2 h_0/g}$) of a single particle decreases as the aspect ratio increases, eventually tends to a
4
5 357 free-fall state.
6

7 358 (3) Gravity levels appear to have minimal effect on deposit run-out distance and final height. The
8
9 359 expected scaling of 1.0 is clearly observed, suggesting that gravity level does not affect the normalized
10
11 360 run-out distance. This conclusion aligns with observations of natural landslides in the Solar System
12
13 361 over a large range of slide geometries. Moreover, the gravity level does not alter the critical aspect ratio
14
15 362 ($a = 1.7$), where a shift occurs in the bilinear relationship. The rescaled final height remains consistent
16
17 363 across various aspect ratio ranges, supported by cross-sectional analysis of deposit profiles for $a = 25$.
18
19 364 Notably, only under high gravity condition (e.g., 10G) was a slight decrease in final height observed,
20
21 365 although the effect was negligible and may be due to small numerical issues.

22 366 (4) Flow mobility was used to quantitatively describe the effect of gravity levels on deposit results. A
23
24 367 modified mobility angle (θ') was proposed to eliminate the effect of the initial geometry (r_0). It was
25
26 368 observed that both θ and θ' decreases as the aspect ratio increases, following the expected scaling of
27
28 369 the gravity level. θ exhibits a small peak point at $a \approx 1$, which is attributed to the effect of initial
29
30 370 geometry. Conversely, the curve of θ' undergoes continuous variation. As aspect ratio increases, the
31
32 371 initial geometry effect diminishes, eventually causing θ' to approach θ .

33 372 (5) Through multiscale studies exploring the genesis of collapse geometry in terms of volume or height
34
35 373 drop, we observed that small scale results (e.g., experiments) are in good agreement with large scale
36
37 374 results (e.g., landslide). Notably, under identical scaling conditions (e.g., identical density, length, etc.),
38
39 375 the extent of collapse appears to be independent of gravity level. Instead, it is found to depend on sample
40
41 376 volume and initial potential energy. The sample volume factor exhibits a clear scale effect, with the
42
43 377 critical point occurring at around $a = 1.7$. Furthermore, both gravitational potential and kinetic energies
44
45 378 demonstrate a good scaling relationship with N , providing additional support for the conclusions drawn
46
47 379 from an energy perspective.

380 381 **CRedit authorship contribution statement**

382 **Yucheng Li:** Conceptualization, Methodology, Validation, Investigation, Writing-original draft.

383 **Bowen Wang:** Conceptualization, Methodology.

384 **Raul Fuentes:** Resources, Writing-review & editing, Supervision.

385 Declaration of Competing Interests

1
2 386 The authors declare that they have no known competing financial interests or personal relationships that
3
4 387 could have appeared to influence the work reported in this paper.
5

6 388 Data availability

7
8 389 Data will be made available on request.
9

10 390 Acknowledgements

11
12
13 391 The first author would like to acknowledge the financial support provided by the China Scholarship
14
15 392 Council for Doctoral Studies no.201808310302.
16

17 393

18 394

19

20 395 Appendix I: SPH artificial viscosity

21
22
23 396 The concept of artificial viscosity was first proposed in one spatial dimension by Ref. (VonNeumann
24
25 397 and Richtmyer, 1950) to model flows with shocks, which is nowadays widely used in wave propagation
26
27 398 programs. The role of the artificial viscosity is to smooth the shock over several particles. The artificial
28
29 399 viscosity term Π_{ij} (Monaghan and Gingold, 1983) is included in the SPH momentum equation as:
30
31

$$32 \frac{Dv_i^\alpha}{Dt} = \sum_{j=1}^N m_j \left(\frac{\sigma_i^{\alpha\beta} + \sigma_j^{\alpha\beta}}{\rho_i \rho_j} + \Pi_{ij} \delta^{\alpha\beta} \right) \frac{\partial W_{ij}}{\partial x_i^\beta} + b_i^\alpha. \quad (23)$$

33
34
35
36 400 where \mathbf{I} is the identity matrix. The most widely used form of artificial viscosity is:
37
38

$$39 \Pi_{ij} = \begin{cases} \frac{-\alpha c_{ij} \phi_{ij} + \beta \phi_{ij}^2}{\rho_{ij}}, & \mathbf{u}_{ij} \cdot \mathbf{x}_{ij} < 0 \\ 0, & \mathbf{u}_{ij} \cdot \mathbf{x}_{ij} \gg 0 \end{cases} \quad (24)$$

$$40 \phi_{ij} = \frac{h_{ij} \mathbf{v}_{ij} \cdot \mathbf{x}_{ij}}{|\mathbf{x}_{ij}^2| + 0.01 h_{ij}^2}, c_{ij} = \frac{c_i + c_j}{2}, \rho_{ij} = \frac{\rho_i + \rho_j}{2}, \quad (25)$$

$$41 h_{ij} = \frac{h_i + h_j}{2}, \mathbf{x}_{ij} = \mathbf{x}_i - \mathbf{x}_j, \mathbf{v}_{ij} = \mathbf{v}_i - \mathbf{v}_j, \quad (26)$$

42
43
44
45 401 where α and β are the problem dependent tuning parameters, and c is the sound speed. J.J.Monaghan
46
47 402 (1994) chose $\alpha = 0.01, \beta = 0$ to simulate the free surface flow. Bui et al. (2007) chose $\alpha = 0.01, \beta = 1$
48
49 403 for water and $\alpha = 1, \beta = 1$ for soil. Here, $\alpha = 0.06$ and $\beta = 1.5$ are chosen based on numerical validation
50
51 404 against the experimental study and direct comparison to J.J.Monaghan (1994) and Bui et al. (2007). The
52
53 405 speed of sound c of the material is calculated according to $c_i = \sqrt{E_i / \rho_i}$. E is the Young's modulus of
54
55 406 the material, assuming isotropic and homogeneous conditions.
56
57
58
59
60

407 Appendix. II: Generalized form of elastic-perfectly plastic model

408 Here, the general form of the elastic-perfectly plastic model is derived. The definition of total strain rate
409 tensor, which can be divided into elastic and plastic parts, as follows:

$$410 \dot{\varepsilon}^{\alpha\beta} = \dot{\varepsilon}_e^{\alpha\beta} + \dot{\varepsilon}_p^{\alpha\beta}, \quad (27)$$

410 where the subscripts e and p present for elastic and plastic components, respectively.

411 The elastic strain rate tensor can be calculated by generalised Hooke's law:

$$412 \dot{\varepsilon}_e^{\alpha\beta} = \frac{\dot{\sigma}^{\alpha\beta}}{2G} + \frac{1}{9K} \dot{\sigma}^{rr} \delta^{\alpha\beta}, \quad (28)$$

412 where $\dot{\varepsilon}^{\alpha\beta}$ is the deviatoric stress rate tensor; G and K are the material shear and bulk modulus; $\delta^{\alpha\beta}$ is
413 the Kronecker's delta.

414 The plastic strain rate tensor can be derived from the plastic flow rule according to:

$$415 \dot{\varepsilon}_p^{\alpha\beta} = \dot{\lambda} \frac{\partial g}{\partial \sigma^{\alpha\beta}}, \quad (29)$$

415 where $\dot{\lambda}$ is the time rate of the plastic multiplier; g is the plastic potential function.

416 Substituting Eqs. (29) and (30) into Eq. (28) and rearranging the obtained equation, the generic form of
417 the elastic-perfectly plastic is given by:

$$418 \dot{\sigma}^{\alpha\beta} = 2G\dot{\varepsilon}^{\alpha\beta} + K\dot{\varepsilon}^{\gamma\gamma}\delta^{\alpha\beta} - \dot{\lambda} \left[\left(K - \frac{2G}{3} \right) \frac{\partial g}{\partial \sigma^{mm}} \delta^{mn} \delta^{\alpha\beta} + 2G \frac{\partial g}{\partial \sigma^{\alpha\beta}} \right], \quad (30)$$

418 where $\dot{\varepsilon}^{\alpha\beta} = \dot{\varepsilon}^{\alpha\beta} - \frac{1}{3}\dot{\varepsilon}^{\gamma\gamma}\delta^{\alpha\beta}$ is the deviatoric strain rate tensor; m and n are free indexes, which are
419 independent from α and β .

420 The plastic multiplier for the elastic-perfectly plastic model can be derived from the consistency
421 condition, which requires the following:

$$422 df = \frac{\partial f}{\partial \sigma^{\alpha\beta}} d\sigma^{\alpha\beta} = 0, \quad (31)$$

422 where f is the yield function that defines the onset of plastic deformation.

423 Substituting Eq. (31) into Eq. (32), the general form of the time rate of the plastic multiplier can be
424 obtained as,

$$425 \dot{\lambda} = \frac{\frac{\partial f}{\partial \sigma^{\alpha\beta}} \left[2G\dot{\varepsilon}^{\alpha\beta} + \left(K - \frac{2G}{3} \right) \dot{\varepsilon}^{\gamma\gamma} \delta^{\alpha\beta} \right]}{2G \frac{\partial f}{\partial \sigma^{mn}} \frac{\partial g}{\partial \sigma^{mn}} + \left(K - \frac{2G}{3} \right) \frac{\partial f}{\partial \sigma^{mn}} \delta^{mn} \frac{\partial g}{\partial \sigma^{mn}} \delta^{mn}}. \quad (32)$$

425 Substituting the Mohr-Coulomb yield function f and its plastic potential function g into Equation (32),
 426 the general form of the plastic multiplier reads the following:

$$\lambda = \frac{1}{H} \left[3K \frac{\partial f}{\partial I_1} \varepsilon^{\gamma\gamma} + 2G \left(\frac{\partial f}{\partial J_2} s^{\alpha\beta} + \frac{\partial f}{\partial J_3} t^{\alpha\beta} \right) \varepsilon^{\alpha\beta} \right], \quad (33)$$

427 where H and $t^{\alpha\beta}$ are defined as follows:

$$H = 9K \frac{\partial f}{\partial I_1} \frac{\partial g}{\partial I_1} + 4GJ_2 \frac{\partial f}{\partial J_2} \frac{\partial g}{\partial J_2} + 6GJ_3 \left(\frac{\partial f}{\partial J_2} \frac{\partial g}{\partial J_3} + \frac{\partial g}{\partial J_2} \frac{\partial f}{\partial J_3} \right) + 2G \left(s^{\alpha m} s^{m\beta} s^{\alpha n} s^{n\beta} - \frac{4}{3} J_2^2 \right) \frac{\partial f}{\partial J_3} \frac{\partial g}{\partial J_3}, \quad (34)$$

$$t^{\alpha\beta} = s^{\alpha m} s^{m\beta} - \frac{2}{3} J_2 \delta^{\alpha\beta}. \quad (35)$$

428

429 References

- 430 ARNDT, T., BRUCKS, A., OTTINO, J. M. & LUEPTOW, R. M. 2006. Creeping granular motion
 431 under variable gravity levels. *Phys Rev E Stat Nonlin Soft Matter Phys*, 74, 031307.
- 432 ATWOOD - STONE, C. & MCEWEN, A. S. 2013. Avalanche slope angles in low - gravity
 433 environments from active Martian sand dunes. *Geophysical Research Letters*, 40, 2929-2934.
- 434 BOWMAN, E. T., LAUE, J., IMRE, B. & SPRINGMAN, S. M. 2010. Experimental modelling of debris
 435 flow behaviour using a geotechnical centrifuge. *Canadian Geotechnical Journal*, 47, 742-762.
- 436 BUI, H. H. & NGUYEN, G. D. 2021. Smoothed particle hydrodynamics (SPH) and its applications in
 437 geomechanics: From solid fracture to granular behaviour and multiphase flows in porous media.
 438 *Computers and Geotechnics*, 138.
- 439 BUI, H. H., SAKO, K. & FUKAGAWA, R. 2007. Numerical simulation of soil–water interaction using
 440 smoothed particle hydrodynamics (SPH) method. *Journal of Terramechanics*, 44, 339-346.
- 441 CABRERA, M. & ESTRADA, N. 2019. Granular column collapse: Analysis of grain-size effects. *Phys
 442 Rev E*, 99, 012905.
- 443 CABRERA, M. & ESTRADA, N. 2021. Is the Grain Size Distribution a Key Parameter for Explaining
 444 the Long Runout of Granular Avalanches? *Journal of Geophysical Research: Solid Earth*, 126.
- 445 CABRERA, M. A., LEONARDI, A. & PENG, C. 2020. Granular flow simulation in a centrifugal
 446 acceleration field. *Géotechnique*, 70, 894-905.
- 447 CABRERA, M. A. & WU, W. 2017. Experimental modelling of free-surface dry granular flows under
 448 a centrifugal acceleration field. *Granular Matter*, 19.
- 449 CAGNOLI, B. & PIERSANTI, A. 2015. Grain size and flow volume effects on granular flow mobility
 450 in numerical simulations: 3-D discrete element modeling of flows of angular rock fragments.
 451 *Journal of Geophysical Research: Solid Earth*, 120, 2350-2366.
- 452 CHEN, W. & QIU, T. 2012. Numerical Simulations for Large Deformation of Granular Materials Using
 453 Smoothed Particle Hydrodynamics Method. *International Journal of Geomechanics*, 12, 127-
 454 135.
- 455 CROSTA, G. B., IMPOSIMATO, S. & RODDEMAN, D. 2009. Numerical modeling of 2-D granular
 456 step collapse on erodible and nonerodible surface. *Journal of Geophysical Research*, 114.

- 457 DORBOLO, S., MAQUET, L., BRANDENBOURGER, M., LUDEWIG, F., LUMAY, G., CAPS, H.,
1 458 VANDEWALLE, N., RONDIA, S., MÉLARD, M., VAN LOON, J., DOWSON, A. &
2 459 VINCENT-BONNIEU, S. 2013. Influence of the gravity on the discharge of a silo. *Granular*
3 460 *Matter*, 15, 263-273.
- 4
5 461 FÁVERO, N., ALOMIR H. & BORJA, R. I. 2018. Continuum hydrodynamics of dry granular flows
6 462 employing multiplicative elastoplasticity. *Acta Geotechnica*, 13, 1027-1040.
- 7
8 463 FERN, E. J. & SOGA, K. 2016. The role of constitutive models in MPM simulations of granular column
9 464 collapses. *Acta Geotechnica*, 11, 659-678.
- 10
11 465 GUE., C. S., BOLTON., K. S. M. & THUSYANTHAN., N. I. 2010. Centrifuge modelling of submarine
12 466 landslide flows. In: *Physical Modelling in Geotechnics-Proceedings of the 7th International*
13 467 *Conference on Physical Modelling in Geotechnics, ICPMG 2010*, 2, 1113-1118.
- 14
15 468 HOANG, U. T. & NGUYEN, N. H. T. 2023. Particle shape effects on granular column collapse using
16 469 superquadric DEM. *Powder Technology*, 424.
- 17
18 470 J.J.MONAGHAN 1994. Simulating Free Surface Flows with SPH. *Journal of Computational Physics*,
19 471 110, 399-406.
- 20
21 472 JING, L., KWOK, C. Y., LEUNG, Y. F., ZHANG, Z. & DAI, L. 2018a. Runout Scaling and Deposit
22 473 Morphology of Rapid Mudflows. *Journal of Geophysical Research: Earth Surface*, 123, 2004-
23 474 2023.
- 24
25 475 JING, L., YANG, G. C., KWOK, C. Y. & SOBRAL, Y. D. 2018b. Dynamics and scaling laws of
26 476 underwater granular collapse with varying aspect ratios. *Physical Review E*, 98.
- 27
28 477 KERMANI, E. & QIU, T. 2018. Simulation of quasi-static axisymmetric collapse of granular columns
29 478 using smoothed particle hydrodynamics and discrete element methods. *Acta Geotechnica*, 15,
30 479 423-437.
- 31
32 480 KLEINHANS, M. G., MARKIES, H., DE VET, S. J., IN 'T VELD, A. C. & POSTEMA, F. N. 2011.
33 481 Static and dynamic angles of repose in loose granular materials under reduced gravity. *Journal*
34 482 *of Geophysical Research*, 116.
- 35
36 483 LAI, Z., JIANG, E., ZHAO, L., WANG, Z., WANG, Y. & LI, J. 2023. Granular column collapse:
37 484 Analysis of inter-particle friction effects. *Powder Technology*, 415.
- 38
39 485 LAI, Z., VALLEJO, L. E., ZHOU, W., MA, G., ESPITIA, J. M., CAICEDO, B. & CHANG, X. 2017.
40 486 Collapse of Granular Columns With Fractal Particle Size Distribution: Implications for
41 487 Understanding the Role of Small Particles in Granular Flows. *Geophysical Research*
42 488 *Letters*, 44.
- 43
44 489 LAJEUNESSE, E., MANGENEY-CASTELNAU, A. & VILOTTE, J. P. 2004. Spreading of a granular
45 490 mass on a horizontal plane. *Physics of Fluids*, 16, 2371-2381.
- 46
47 491 LAJEUNESSE, E., MONNIER, J. B. & HOMSY, G. M. 2005. Granular slumping on a horizontal
48 492 surface. *Physics of Fluids*, 17, 103302.
- 49
50 493 LAJEUNESSE, E., QUANTIN, C., ALLEMAND, P. & DELACOURT, C. 2006. New insights on the
51 494 runout of large landslides in the Valles - Marineris canyons, Mars. *Geophysical Research*
52 495 *Letters*, 33.
- 53
54 496 LI, Y., WEI, D., ZHANG, N. & FUENTES, R. 2024. Effect of basal friction on granular column
55 497 collapse. *Granular Matter*, 26.
- 56
57 498 LUBE, G., HUPPERT, H. E., SPARKS, R. S. J. & HALLWORTH, M. A. 2004. Axisymmetric
58 499 collapses of granular columns. *Journal of Fluid Mechanics*, 508, 175-199.
- 60
61 500 LUCAS, A., MANGENEY, A. & AMPUERO, J. P. 2014. Frictional velocity-weakening in landslides
62 501 on Earth and on other planetary bodies. *Nat Commun*, 5, 3417.

- 502 LUCAS, A., MANGENEY, A., MÈGE, D. & BOUCHUT, F. 2011. Influence of the scar geometry on
1 503 landslide dynamics and deposits: Application to Martian landslides. *Journal of Geophysical*
2 504 *Research*, 116.
- 3
4 505 MAN, T., HUPPERT, H. E., LI, L. & GALINDO-TORRES, S. A. 2021a. Deposition morphology of
5 506 granular column collapses. *Granular Matter*, 23.
- 6
7 507 MAN, T., HUPPERT, H. E., LI, L. & GALINDO-TORRES, S. A. 2021b. Finite-Size Analysis of the
8 508 Collapse of Dry Granular Columns. *Geophysical Research Letters*, 48.
- 9
10 509 MANGENEY, A., ROCHE, O., HUNGR, O., MANGOLD, N., FACCANONI, G. & LUCAS, A. 2010.
11 510 Erosion and mobility in granular collapse over sloping beds. *Journal of Geophysical Research*,
12 511 115.
- 13 512 MARSHALL, J. P., HURLEY, R. C., ARTHUR, D., VLAHINIC, I., SENATORE, C., IAGNEMMA,
14 513 K., TREASE, B. & ANDRADE, J. E. 2018. Failures in sand in reduced gravity environments.
15 514 *Journal of the Mechanics and Physics of Solids*, 113, 1-12.
- 16
17 515 MERUANE, C., TAMBURRINO, A. & ROCHE, O. 2010. On the role of the ambient fluid on
18 516 gravitational granular flow dynamics. *Journal of Fluid Mechanics*, 648, 381-404.
- 19
20 517 MONAGHAN & GINGOLD, R. A. 1983. Shock Simulation by the Particle Method of SPH. *Journal*
21 518 *of Computational Physics*, 52, 374-389.
- 22
23 519 NAKASHIMA, H., SHIOJI, Y., KOBAYASHI, T., AOKI, S., SHIMIZU, H., MIYASAKA, J. &
24 520 OHDOI, K. 2011. Determining the angle of repose of sand under low-gravity conditions using
25 521 discrete element method. *Journal of Terramechanics*, 48, 17-26.
- 26
27 522 P. G. HOFMEISTER, J. B. A. D. H. 2009. The Flow Of Granular Matter Under Reduced-Gravity
28 523 Conditions. *AIP Conference Proceedings*, 1145.
- 29
30 524 POLANÍA, O., CABRERA, M., RENOUF, M. & AZÉMA, E. 2022. Collapse of dry and immersed
31 525 polydisperse granular columns: A unified runout description. *Physical Review Fluids*, 7,
32 526 084304.
- 33
34 527 ROCHE, O., ATTALI, M., MANGENEY, A. & LUCAS, A. 2011. On the run-out distance of
35 528 geophysical gravitational flows: Insight from fluidized granular collapse experiments. *Earth*
36 529 *and Planetary Science Letters*, 311, 375-385.
- 37
38 530 SHEIKH, B., QIU, T. & AHMADIPUR, A. 2021. Comparison of SPH boundary approaches in
39 531 simulating frictional soil–structure interaction. *Acta Geotechnica*, 16, 2389-2408.
- 40
41 532 STROM, A., LI, L. & LAN, H. 2019. Rock avalanche mobility: optimal characterization and the effects
42 533 of confinement. *Landslides*, 16, 1437-1452.
- 43
44 534 SU, D., ZHANG, R., LEI, G. & LI, Q. 2022. Experimental and numerical study on collapse of quasi-
45 535 two-dimensional bilayer granular column. *Advanced Powder Technology*, 33.
- 46
47 536 SZEWC, K. 2017. Smoothed particle hydrodynamics modeling of granular column collapse. *Granular*
48 537 *Matter*, 19.
- 49
50 538 TAPIA-MCCLUNG, H. & ZENIT, R. 2012. Computer simulations of the collapse of columns formed
51 539 by elongated grains. *Phys Rev E Stat Nonlin Soft Matter Phys*, 85, 061304.
- 52
53 540 TENG MAN, H. E. H. 2022. Man Teng Influence of Cross-section Shape on Granular Column. *Powder*
54 541 *Technology*.
- 54
55 542 THOMPSON, E. L. & HUPPERT, H. E. 2007. Granular column collapses: further experimental results.
56 543 *Journal of Fluid Mechanics*, 575, 177-186.
- 57
58 544 VONNEUMANN, J. & RICHTMYER, R. D. 1950. A Method for the Numerical Calculation of
59 545 Hydrodynamic Shocks. *Journal of Applied Physics*, 21, 232-237.
- 60
61
62
63
64
65

546 WARNETT, J. M., DENISSENKO, P., THOMAS, P. J., KIRACI, E. & WILLIAMS, M. A. 2014.
1 547 Scalings of axisymmetric granular column collapse. *Granular Matter*, 16, 115-124.
2
3 548 WEI, D., WANG, J., NIE, J. & ZHOU, B. 2018. Generation of realistic sand particles with fractal nature
4 549 using an improved spherical harmonic analysis. *Computers and Geotechnics*, 104, 1-12.
5 550 YANG, E., BUI, H. H., DE STERCK, H., NGUYEN, G. D. & BOUAZZA, A. 2020. A scalable parallel
6 551 computing SPH framework for predictions of geophysical granular flows. *Computers and*
7 552 *Geotechnics*, 121.
8
9 553 ZHANG, R., SU, D., LEI, G. & CHEN, X. 2021. Three-dimensional granular column collapse: Impact
10 554 of column thickness. *Powder Technology*, 389, 328-338.
11
12 555 ZHU, R., HE, Z., ZHAO, K., VOWINCKEL, B. & MEIBURG, E. 2022. Grain-resolving simulations
13 556 of submerged cohesive granular collapse. *Journal of Fluid Mechanics*, 942.
14

15 557

16
17
18
19
20
21
22
23
24
25
26
27
28
29
30
31
32
33
34
35
36
37
38
39
40
41
42
43
44
45
46
47
48
49
50
51
52
53
54
55
56
57
58
59
60
61
62
63
64
65

Declaration of interests

The authors declare that they have no known competing financial interests or personal relationships that could have appeared to influence the work reported in this paper.

The authors declare the following financial interests/personal relationships which may be considered as potential competing interests:

Yucheng LI reports financial support was provided by China Scholarship Council. If there are other authors, they declare that they have no known competing financial interests or personal relationships that could have appeared to influence the work reported in this paper.

Dear Editor-in-Chief,

We are pleased to submit our manuscript, titled “Granular column collapse: Analysing the effects of gravity levels”, for consideration for publication in *Computers and Geotechnics*.

In this study, we investigate how varying gravity levels impact the collapse dynamics of granular columns using the Smoothed Particle Hydrodynamics (SPH) method. Our findings demonstrate that gravity significantly accelerates the collapse process, although it does not alter the deposit run-out distance and final height across different gravity levels. This conclusion is further supported by observational data from natural landslides across the Solar System, demonstrating that the spread range of collapsed material is governed more by sample volume and initial potential energy than by gravity alone.

Our study offers new insights into the collapse mechanisms of granular materials, with implications for planetary exploration and modelling natural geotechnical phenomena under different gravitational conditions. We believe that our findings will be of interest to the readership of *Computers and Geotechnics*, especially those engaged in numerical modelling of granular materials and planetary geotechnics.

Thank you for considering our submission. We look forward to your feedback.

Sincerely,

Yucheng LI